NAVAL POSTGRADUATE SCHOOL

MONTEREY, CALIFORNIA

THESIS

STRESS-STRAIN RELATIONSHIPS IN ULTRA-HIGH MOLECULAR WEIGHT POLYETHYLENE FIBERS UNDER BALLISTIC LOADING

by

Matthew Walker

June 2018

Thesis Advisor: Raymond M. Gamache
Second Reader: Peter Crooker

THIS PAGE INTENTIONALLY LEFT BLANK

REPORT DOCUMENTATION PAGE			*Form Approved OMB No. 0704-0188*

1. AGENCY USE ONLY *(Leave blank)*	**2. REPORT DATE** June 2018	**3. REPORT TYPE AND DATES COVERED** Master's thesis

4. TITLE AND SUBTITLE STRESS-STRAIN RELATIONSHIPS IN ULTRA-HIGH MOLECULAR WEIGHT POLYETHYLENE FIBERS UNDER BALLISTIC LOADING	**5. FUNDING NUMBERS**
6. AUTHOR(S) Matthew Walker	
7. PERFORMING ORGANIZATION NAME(S) AND ADDRESS(ES) Naval Postgraduate School Monterey, CA 93943-5000	**8. PERFORMING ORGANIZATION REPORT NUMBER**
9. SPONSORING / MONITORING AGENCY NAME(S) AND ADDRESS(ES) N/A	**10. SPONSORING / MONITORING AGENCY REPORT NUMBER**

11. SUPPLEMENTARY NOTES The views expressed in this thesis are those of the author and do not reflect the official policy or position of the Department of Defense or the U.S. Government.

12a. DISTRIBUTION / AVAILABILITY STATEMENT Approved for public release. Distribution is unlimited.	**12b. DISTRIBUTION CODE** A

13. ABSTRACT (maximum 200 words)

Ultra-high molecular weight polyethylene (UHMWPE) fibers are commonly used in body armor systems, alone or in combination with ceramic inserts, as ballistic protection against high-velocity projectiles. Under dynamic loading conditions, the fibers are extremely strong in tension, but the extreme pressures created at impact by ogive-shaped projectiles can cause premature failure before additional fibers can be recruited to distribute the force. A light gas gun was used to launch 9.525 mm steel spherical projectiles into a sample of 20 layered UHMWPE uniaxial fiber sheets (at 90-degree offset between layers) to examine the stress/strain behavior of the fabric over time. Load cells (4.4 kN) were used to measure uniaxial forces along the fibers. Two high-speed video cameras were used to measure both the in-plane and out-of-plane fiber deflection. Using numerical calculations of the total strain, stress was derived from published stress-strain curves and compared to the measured load cell force data, in both X and Y directions.

14. SUBJECT TERMS UHMWPE, ballistic, body armor	**15. NUMBER OF PAGES** 53
	16. PRICE CODE

17. SECURITY CLASSIFICATION OF REPORT	**18. SECURITY CLASSIFICATION OF THIS PAGE**	**19. SECURITY CLASSIFICATION OF ABSTRACT**	**20. LIMITATION OF ABSTRACT**
Unclassified	Unclassified	Unclassified	UU

NSN 7540-01-280-5500 Standard Form 298 (Rev. 2-89) Prescribed by ANSI Std. 239-18

THIS PAGE INTENTIONALLY LEFT BLANK

Approved for public release. Distribution is unlimited.

STRESS-STRAIN RELATIONSHIPS IN ULTRA-HIGH MOLECULAR WEIGHT POLYETHYLENE FIBERS UNDER BALLISTIC LOADING

Matthew Walker
Major, Canada Army
BS, Carleton University, 2002

Submitted in partial fulfillment of the
requirements for the degree of

MASTER OF SCIENCE IN APPLIED PHYSICS

from the

NAVAL POSTGRADUATE SCHOOL
June 2018

Approved by: Raymond M. Gamache
Advisor

Peter Crooker, Professor Emeritus
Second Reader

Kevin B. Smith
Chair, Department of Physics

THIS PAGE INTENTIONALLY LEFT BLANK

ABSTRACT

Ultra-high molecular weight polyethylene (UHMWPE) fibers are commonly used in body armor systems, alone or in combination with ceramic inserts, as ballistic protection against high-velocity projectiles. Under dynamic loading conditions, the fibers are extremely strong in tension, but the extreme pressures created at impact by ogive-shaped projectiles can cause premature failure before additional fibers can be recruited to distribute the force. A light gas gun was used to launch 9.525 mm steel spherical projectiles into a sample of 20 layered UHMWPE uniaxial fiber sheets (at 90-degree offset between layers) to examine the stress/strain behavior of the fabric over time. Load cells (4.4 kN) were used to measure uniaxial forces along the fibers. Two high-speed video cameras were used to measure both the in-plane and out-of-plane fiber deflection. Using numerical calculations of the total strain, stress was derived from published stress-strain curves and compared to the measured load cell force data, in both X and Y directions.

THIS PAGE INTENTIONALLY LEFT BLANK

TABLE OF CONTENTS

THIS PAGE INTENTIONALLY LEFT BLANK

LIST OF FIGURES

THIS PAGE INTENTIONALLY LEFT BLANK

LIST OF TABLES

THIS PAGE INTENTIONALLY LEFT BLANK

LIST OF ACRONYMS AND ABBREVIATIONS

BFD	back face deformation
DIC	digital image correlation
HB26	variant of the Dyneema brand fibers used in this experiment
LabVIEW	Laboratory Virtual Instrument Engineering Workbench
NPS	Naval Postgraduate School
PTFE	Polytetrafluoroethylene
RTP	resistance to penetration
SAPI	small arms protective insert
TEMA	TrackEye Motion Analysis software by Image Systems
UHMWPE	ultra-high molecular weight polyethylene
V_{50}	ballistic resistance limit[1]

[1] A material property defined as the velocity at which a given projectile mass, geometry, and angle of obliquity has a 50% chance of penetrating a target sample of given composition and areal density.

THIS PAGE INTENTIONALLY LEFT BLANK

I. INTRODUCTION

High tensile strength fabric and fiber-reinforced composite materials are frequently used in body armor systems because of their strong impact resistance and lightweight. They can be used independently for low velocity blunt-tip threats, or combined with ceramic front-face plates (SAPI) as a composite system with improved mass efficiency over ceramic materials alone.

In all armor systems, design concepts attempt to mitigate the incident pressure of the projectile. Two key methods exist to reduce the incident pressure: increasing the projectile impact surface area or decreasing the deceleration forces through prolongation of the arresting time period. Current SAPI technologies employ both techniques; a ceramic face is used to blunt the incident threat; and a textile system whose tensile strength under deformation arrests the projectile over a prolonged period of time compared to traditional metal armor.

Textile armor systems are extremely mass efficient but require incident projectiles to exhibit pressures below a certain threshold to avoid immediate local fiber breakage. If this threshold is exceeded, the incident projectile will penetrate the textile armor system with minimal loss in energy. If a composite armor system is designed well, a proper handover of the incident projectile will occur to the textile matrix at pressures below the threshold limit. With the assumption that ceramic material adequately blunts/breaks up the incident projectile, it can be arrested using an adequate number of ballistic fiber layers based on the residual velocity and impact surface area. A better comprehension of the physical response in fabrics, and the characteristic alterations used in manufacturing (application of temperature and pressure conditioning), should lead to improvement in the mass efficiency of armor systems.

Research into the ballistic performance of fabrics has typically fallen into two distinct categories: empirical data collected from destructive testing under impact loading conditions, and analytic models that use wave front velocities or energy equations to try and simulate material behavior. A knowledge gap exists between simple analytic models,

which do not sufficiently account for the variation in material properties, and failure mechanisms.

This research seeks to develop an experimental tool for the evaluation of textile armor systems under ballistic impact, using stress-strain relationships. Within this study, 9.525 mm steel spheres are impacted into uniaxial sheets of Dyneema HB26 fibers, oriented in a 0°/90° configuration. An experimental apparatus will enable both stress and strain measurements of the fiber system. The test system will include two separate load cells, each dedicated to a separate uniaxial direction, and a stereographic imaging system to measure the deformation during an impact event. With this method, fiber systems can be studied for both dynamic material response and failure mechanics.

II. BACKGROUND

A. HISTORY OF BODY ARMOR

Personal body armor has played a significant role in armed conflict for centuries. Medieval knights and ancient Japanese warriors would use chainmail, forged iron breastplates, and even wooden slats to protect soft tissue from the slashing and piecing effects of swords and spears. As advances were made in weaponry, so changed the fundamental design of body armor. The principle threat switched from slow cutting and slashing motions to high-velocity projectiles. As technology improved to match the threat, additional factors began to dominate design including areal density, mobility, material availability and cost.

Around the time of the Second World War, composite personal armor systems emerged, like the combination of Doron (a polyester-glass fabric laminate with high retardation effect) and nylon cloth, which demonstrated a high mass efficiency compared to monolithic designs. Fiber based systems offered the advantage of both reduced weight and flexibility. In the mid-1960s, Kevlar became the leading fabric in personal body armor systems. By the late 1990s, UHMWPE fibers such as Dyneema and Spectrashield would emerge for their superior V_{50} performance. The current design of most personal body armor systems consists of two main components: a carrier vest with a Kevlar multilayer liner, and ceramic ballistic plate backed by UHMWPE fiber [1].

B. CHALLENGES

With the variation in threats that exist for personal body armor, it is important to design a system with consideration for each threat independently. Similarly, the dual nature of a composite armor system requires a detailed knowledge of each constituent component to facilitate optimal integration. Typically, the front-face ceramic is responsible to both break up and blunt the projectile and decrease the incident velocity. The change in the incident projectile shape and velocity affects the interaction with the backing material and determines whether the projectile will, or will not, penetrate the backing material.

The ability to quantify the required performance of both the front-face and backing material will assist the design process for armor systems based on specific threats. Specifically, a method to better understand the interaction of the textile backing system with a projectile can better support performance requirements specific only to the front-face armor system. Because fibers such as Kevlar and Dyneema have been in use for decades, there is a large amount of testing data available regarding V_{50} performance for a variety of projectile types, fabric matrix configurations and areal densities. While much is known about the ballistic performance of specific fibers, there are still many areas where the knowledge base is weak. Specifically, the dynamic interaction of backing material systems based on variations in projectile type, incident velocity, fabrication pressure, and boundary conditions, require further study.

Recent tests at NPS have shown that for a new type of armor incorporating ceramic spheres, traditional high-performance textile backing materials do not respond consistent with those in conventional monolithic ceramic systems [2]. An improved method for quantifying the coupling of the ballistic impact to the textile system is required to better understand when failure occurs and what variables affect failure propagation. There is currently a need for the ability to measure the physical performance of fabrics under dynamic loading, specifically a better understanding of when failure occurs and what variables affect failure propagation.

The key challenge is to develop an improved method of quantifying the coupling of the ballistic impact to the textile system. Specifically, a capability is required that can measure the stress/strain response of fibers under dynamic conditions. This quantification will enable a thorough investigation of the system variables (fiber type, temperature and pressing conditions, quality) as well as performance subjected to different projectile shapes and velocities.

C. ANALYTIC AND EMPIRICAL MODELS

The first step in any analytic model depicting the behavior of fabric under impact loading is to consider the effect of projectile impact on a single fiber strand subject to transverse loading. A simple analytic solution to this problem was developed by Smith in

1958 [3]. In his model, fibers are treated as infinite in length and not subjected to clamping or boundary conditions at their endpoints. This means that wave propagation, in this case a series of wavelets moving outward immediately following impact, can be analyzed without concern for the reflection of waves at the boundary. Smith, building on the work of von Karman [4], identified three critical wave fronts moving along the fiber that can be used to identify characteristic regions of material behavior.

The elastic wave front separates the region of fiber at rest, unaware that an impact had occurred, from the region already experiencing material strain. In the wake of the elastic wave front material flows inward, and with the passing of each subsequent wavelet there is an increase in the velocity of the material flow and the effective strain. The final wavelet is known as the plastic wave front. All material in the wake of the plastic wave flows at a constant velocity and maintains a constant strain. The transverse wave separates material that moves only in the longitudinal direction, from material that begins to move in the transverse direction, forming a tent-like shape in the material. For low impact velocities, the transverse wave is slower than the plastic wave, and material in its wake moves only in the transverse direction, with the angle formed by the tent remaining constant during propagation. At high impact velocities the transverse wave can overtake the plastic wave, and strain rates vary inside the tent. In this case the angle made between the tent edge and the longitudinal axis of the fiber will also change over time. A representation of the waves propagating through a single fiber can be seen in Figure 1.

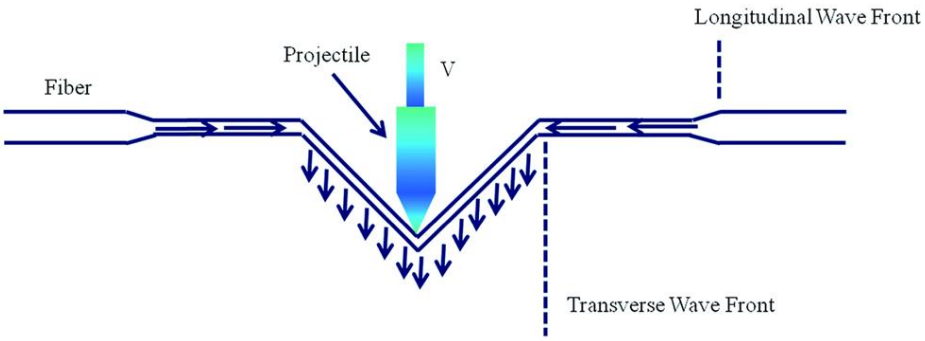

Figure 1. Wave Propagation—Single Filament. Source: [5].

Research conducted by Sanborn [6] produced high-rate stress-strain curves (Figure 2) showing that fibers in tension demonstrate a consistent behavior until loading conditions exceed the tensile strength.

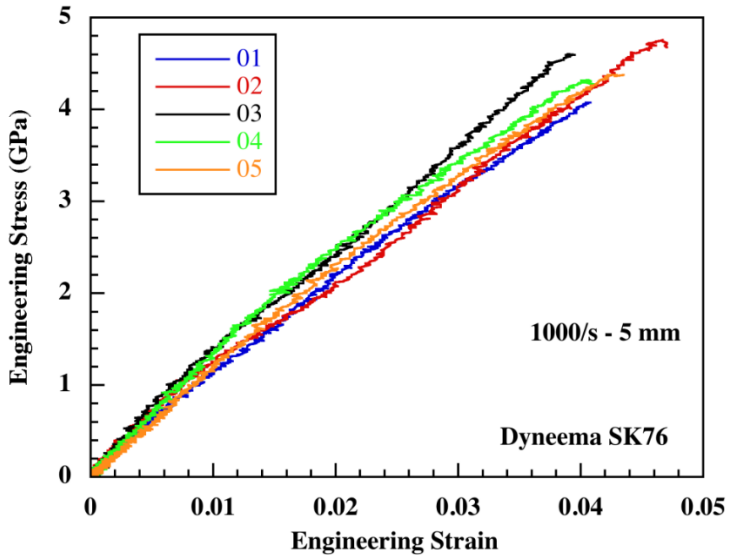

Figure 2. Stress-strain Relationship in UHMWPE. Source: [6].

The analytical model developed by Smith was scalable for multiple fibers acting in the same direction, but did not account for the behavioral characteristics of woven fabrics with interlocking weaves, nor did it address the effects of strand breakage after impact. A refined model was developed by Chocron-Benloulo [7] that built on the transverse wave velocity formula from the Smith model and determined a damage coefficient that would resolve the energy losses to breakage missing from the Newton momentum equation. In his model, the energy lost by the projectile is accounted for by scaling the kinetic energy transferred to the fiber matrix with the damage coefficient. This model was still limited by the assumptions that the fabric behaves unidirectionally, and the strain and projectile velocity are constant. This reduced the impact force in the transverse direction to a function of strain, number of fibers exposed to surface impact, number of fiber layers, and the cross section of the fibers. The resulting damage coefficient was treated as a material property

and generated by matching the model to experimental results at the ballistic limit (evaluating the equation at V_{50} and applying a fit parameter).

Further research was conducted by Tan [8] to examine how ballistic limits, energy absorption and damage compared when fabrics were subjected to projectiles of different shape. In general, Tan categorized performance using three regimes: impact below the ballistic limit, low velocity perforation, and high velocity perforation. For impacts below the ballistic limit, energy absorption was proportional to the impact velocity. Severe geometries, such as ogive and conical projectiles, performed the worst due to the extreme pressure they create with such a small strike area at initial impact. Cylindrical and spherical shapes demonstrated higher energy absorption since the impact was distributed over a larger number of fibers resulting in lower pressure and fewer strands exceeding tensile strength prior to the expansion of the transverse wave tent. Tan also noted that the samples that showed the highest deformation were those with the highest energy absorption.

Ballistic performance is also affected by orientation of the fiber layers, and the manufacturing process used in constructing the matrix. In a study conducted by Vargas-Gonzalez [9], processing temperature and pressure were varied to determine their impact on BFD (total deflection) and RTP (V_{50}). Samples showed extreme sensitivity to processing temperature, directly reducing BFD until a minimum value at 135 °C, regardless of pressure. At the same time, increased pressure during the manufacturing process resulted in higher V_{50} performance.

THIS PAGE INTENTIONALLY LEFT BLANK

III. EXPERIMENTAL SETUP

A. SYSTEM DESIGN

Experimental determination of the stress-strain relationship requires two principal data sets: uniaxial force measurements of the tension applied to the UHMWPE fibers, and deflection measurements of the sample in the direction of impact. In this experiment, 9.525 mm spherical chromium steel ball-bearing projectiles were launched at speeds focussed at 305 m/s into a target composed of 20 layers of UHMWPE fiber oriented in a 0° - 90° configuration. The target sample was mounted perpendicular to the flightpath (labeled as the Z direction) with fibers clamped longitudinally in the horizontal direction (0° - labeled as the X direction) and the vertical direction (90° - labeled as the Y direction). Strain gauge load cells were used to determine the tensile force applied to the fibers in both the X and Y directions. A trigger mechanism was used to synchronize the force measurements with two high-speed cameras that would capture the impact deformation of the target sample from behind the target mount. DIC software was used to determine the deflection of the fibers at the same sampling rate as the force measurement (50 kHz). A view of the gas gun facility, including the target and camera configuration, can be seen in Figure 3.

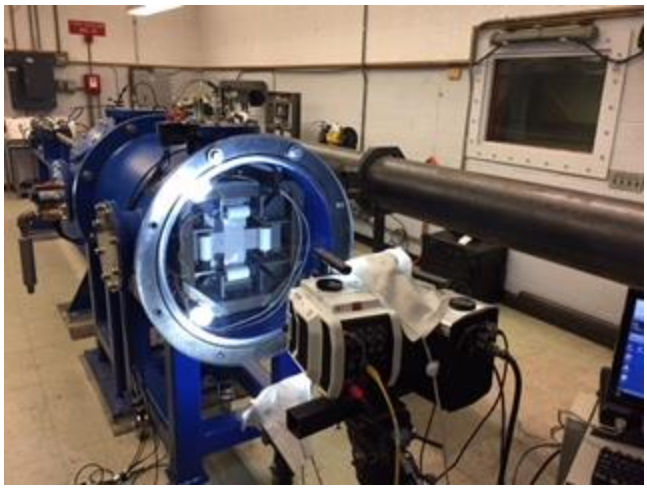

Figure 3. Gas Gun Facility

The experimental setup can be broken down into three principle groups: the physical system of components that interact directly with the projectile, the control systems that operate and synchronize devices, and the data collection equipment to measure and record results. Figure 4 is a system diagram showing the linkages of individual components with projectile physical interactions shown in solid red, data transfer paths shown in dotted red and control functions shown in green.

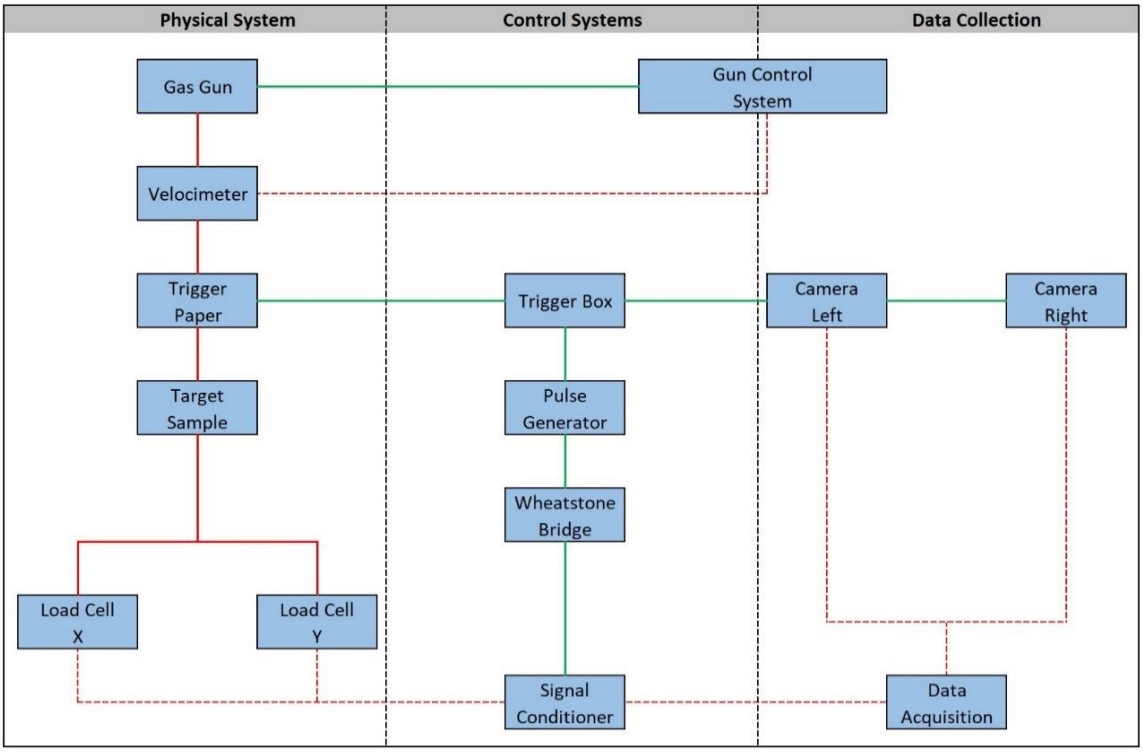

Figure 4. System Diagram

B. PHYSICAL SYSTEM

The principle component of the physical system is the light gas gun (Figure 5), manufactured by Physics Applications Inc. The gun uses compressed dry air for both projectile acceleration and fire control. The system is charged by pressurizing the breech to the required level to achieve the desired projectile speed. The breech is sealed by a piston that acts as the principle firing mechanism. To launch the projectile, sufficient pressure is

applied to the piston to expose the breech pressure to the barrel, driving the sabot and enclosed projectile towards the target. The system is capable of operating at pressures between 0 and 42 MPa. Projectiles can be launched with repeatable speeds between 100 m/s and 1200 m/s. The barrel has a smooth bore with an inner diameter of 25.4 mm and is capable of firing a variety of projectiles including both spherical and ogive shapes.

Figure 5. Gas Gun—Breech View

The steel spheres were launched in 3-D printed polycarbonate sabots. The sabots serve to encapsulate the sphere and maintain its position while traveling down the gun barrel as well as providing a tight fit to prevent gas blow-by during the acceleration down the barrel. Once free from the barrel, the projectile passes through a laser velocimeter before the sabot is stripped prior to impact with the target. Inside the velocimeter, paired sets of lasers and photodetector are used to record the passing of the projectile between each of the three gates. The software records the change in voltages from the photodetector when the projectile breaks the laser beam aligned to the active area of the detector cell. The sampling rate of the data acquisition card is 2.5 million samples per second. Because the distances are known between each laser, the time indexes of the voltage changes can be used to calculate the speed of the projectile.

A receiving chamber and catch tank are used to both study ballistic events and arrest the projectile and target spall after the impact study is performed. The catch tank is backed by 20 6.35 mm ASTM-36 steel plates stacked in series. The target mounting area is contained within a 61 cm (inner diameter) cylinder which can support a variety of target configurations. There are viewing portals on each side of the target area for high speed projectile motion capture. At low projectile speeds the catch tank can be removed and replaced with a set of polycarbonate windows for rear facing views of the target.

Targets were constructed using thin, 13” long, 3” wide sheets of Dyneema HB26 [10] UHMWPE, arranged in a single ply with a common longitudinal fiber direction (Figure 6). Plies were then mounted in alternating 0° and 90° orientations forming a 20 layer cross-shaped target sample. Targets were assembled using a specially designed jig that properly aligns the HB26 samples in both the X and Y directions (Figure 7). Clamps identical to those used in the target mount pre-form the target surface to the required shape for mounting. Nolax adhesive film was inserted between each individual layer at the clamping site to prevent slippage of the fibers. HMVK polyuria was applied to the exterior to prevent shearing of the fibers by the clamp during impact loading. Prior to pressing, the targets were heated in an oven at 135 °C for a period of two hours. Heated targets were placed a hydraulic press at values of 6.9 MPa, 13.8 MPa and 20.7 MPa, and held at the specified pressure for five minutes.

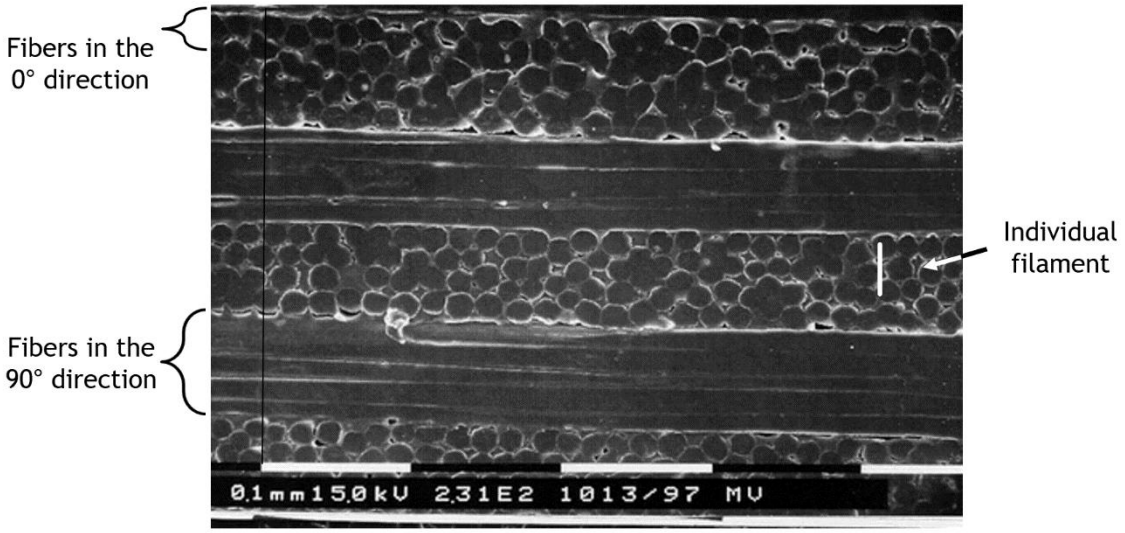

Figure 6. UHMWPE Fiber Cross Section. Source: [10].

Figure 7. Target Fabrication Jig

Target samples for DIC analysis were imprinted using an inkjet printer with a speckle pattern (Figure 8) of dots on the fiber plies exposed to the rear facing high-speed cameras. This pattern was designed so that the dots form patterns roughly 3-5 pixels wide that can be identified by each camera as a unique feature.

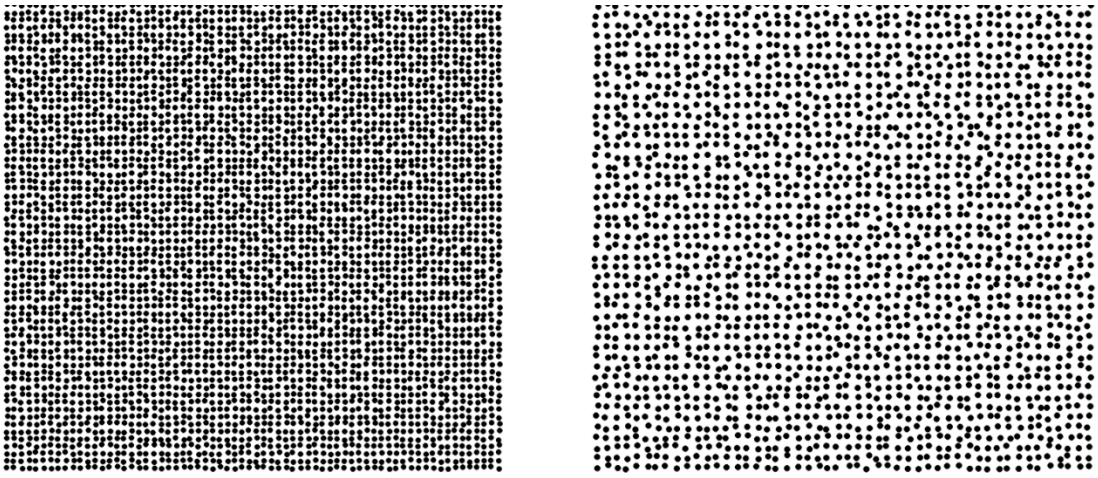

(a) Dense Pattern (b) Sparse Pattern

Figure 8. DIC Speckle Pattern

The target mount was designed to clamp samples down creating a fixed boundary condition at the end-points of fiber strands. This facilitates force measurements to be taken uniaxially. Mounting the apparatus upright in the receiving chamber aligns the X and Y directions to horizontal and vertical with respect to the ground. Figure 9 shows the orientation of a sample in the mount. In each loading direction, a clamp is attached to an Omega LCHD-1k [11] strain-gauge load cell, capable of measuring applied forces from 0 to 4.4 kN. As the target sample is deformed in the Z direction during projectile impact, PTFE frictionless rollers[2] convert the tensile force to the X and Y direction for measurement.

[2] The rollers were constructed from PTFE and mounted on roller bearing with a negligible friction coefficient relative to the forces applied to the load cell. The system is not "frictionless" in absolute terms but does transfer the forces to the X and Y direction with minimal losses.

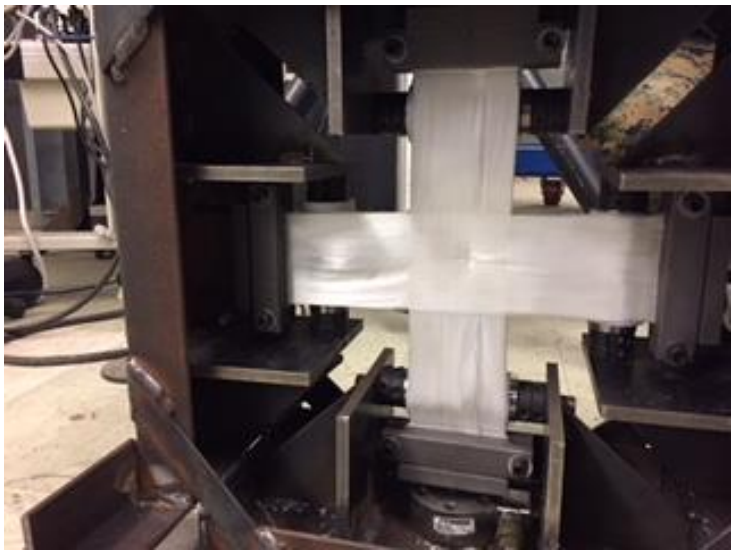

Figure 9. Target Mount

To initiate both the high-speed cameras and load cells, a trigger mechanism was placed in front of the fiber target. The trigger system incorporated a break screen placed approximately 3 cm directly in front of the target. When the break screen is impacted, a trigger box detects the change in the conduction path and generates a 5 V square wave to activate all instrumentation prior to the actual impact of the projectile with the target.

C. CONTROL SYSTEMS

The gas gun is controlled by a software program created using National Instruments LabVIEW. A series of control switches were coded into the program and used to operate solenoids and valves on the test apparatus that control breech pressure, firing valve pressure, and the reset valve. The system can be charged/purged automatically or by manually operating each switch independently. The system can be set for pressures between 2 MPa and 42 MPa with increments of 0.007 MPa. Testing has been conducted at 2 MPa and 17 MPa with consistent speeds in the range of 305 m/s (+/- 15 m/s) and 915 m/s (+/- 30 m/s), respectively. Pressures below 2 MPa are possible, but have not been tested for system repeatability. The control system for the gas gun is located in a separate room from the physical apparatus for maximum safety (Figure 10).

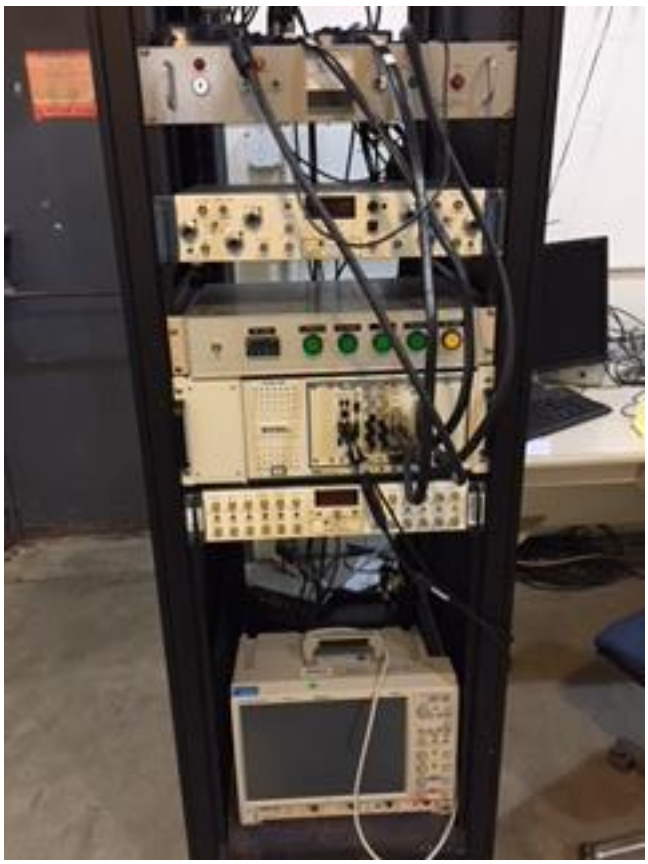

Figure 10. Gas Gun Control System

A separate control system is used to activate and synchronize the high-speed cameras and load cell data acquisition. The trigger paper is connected to a Whithner Triggerbox 1000 [12] that outputs a +5V signal when the break-screen conduction is broken by the projectile. This activates the trigger input on each high-speed camera, and the Berkeley Nucleonics 577 pulse generator [13] (Figure 11). Because the load cell data acquisition card cannot receive an external trigger, a technique was developed to time index the trigger event. At the moment of projectile impact, a software trigger of the load cell data acquisition system occurs. Unfortunately, this software trigger incorporates a large delay compared to the actual trigger of the break screen. The pulse generator is used to send a square-wave to the load cell data acquisition system via a fictitious force signal as a third input measurement. By setting a known pulse-width (1ms), the falling edge of the square-wave is used to synchronize the load cell data with the high-speed cameras. The pulse signal is input into a Wheatstone bridge circuit (Figure 12) to simulate a third load

cell input to the data acquisition system. A National Instruments NI9237 signal conditioner and data acquisition card [14] (Figure 13) provides +10V excitation to the load cells and outputs the force readings to the measurement software.

Figure 11. Pulse Generator

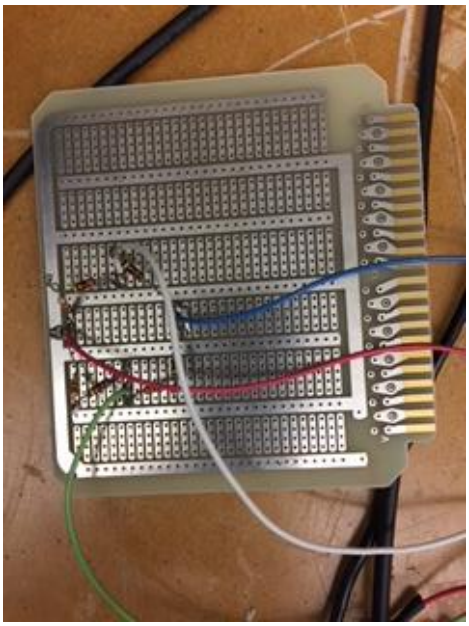

Figure 12. Wheatstone Bridge

Figure 13. Data Acquisition Card

D. DATA COLLECTION AND PROCESSING

Three sets of data are recorded for each target sample tested: velocimeter voltage data, for the calculation of projectile speed; load cell voltage output, for the calculation of tensile forces in the X and Y directions; and, image files, for input into the DIC software to determine deflection in the Z direction.

The load cell output voltages are amplified through the data acquisition card and recorded using a LabVIEW program that stores the information at a 50 kHz sampling rate with 24-bit resolution. The output data file contains values for both X and Y load cells at each time step, and is calibrated in units of force. The pulse data is also captured for synchronization purposes, and when its value drops to zero the time-step index is known to correspond with an actual time of 1ms post-trigger activation.

High-speed cameras are used to record deformation of the target samples in the Z direction. During testing, the cameras were set to record 10 μs exposures at 50,000 fps, which matched the 50 kHz sampling rate of the load cell force measurements. The original configuration used a Phantom V2512 [15] (512:320 resolution at 28 μm pixel size) and a Shimadzu HPV-X2 [16] (400:250 resolution at 32 μm pixel size). A second configuration consisted of the original Phantom V2412 (set to 256:256 resolution at 28 μm pixel size) paired with a Phantom V711 [17] (256:256 resolution at 20 μm pixel size). Calibration images used to confirm camera orientation were recorded for each target configuration.

TEMA DIC software is used to convert the image files into deflection data that can be used to calculate strain in the fibers. The software works by comparing the left and right camera images frame-by-frame and as the speckle pattern deforms, the software extrapolates where the point is in 3-D space.

A secondary mechanism was employed to measure deflection for cases where the distortion of the material exceeded the ability of the DIC software to track movement of the unique speckle patterns. A mirror was set on the fabric at a 45° angle so that a high-speed camera could be used to view the Z direction from an offset position. Measurements were calibrated by placing a sample of known height at various positions between the mirror and deflection ruler to ensure there was no parallax in the setup.

E. NUMERICAL SIMULATION

The force measurements obtained experimentally can be verified against the theoretical predictions of Smith [3] by converting the total strain observed into a force calculation using the stress-strain results from Sanborn [6]. In cases where the complete deflection profile produced using DIC is unavailable, the transverse deformation can be approximated using numerical simulation. A software package was developed in LabVIEW that uses the image data of the deformation tent to determine the change in individual fiber length which can be summed over the entire sample to produce the total strain in each image frame. Converting strain to force also takes into consideration the number of material layers as well as the number-density of filaments in the cross section of each layer. Total force can be computed separately for the X and Y directions for comparison with the load cell data.

To generate the deformation profile, the software program uses location data for the vertices at the base of the tent and the deflection measurement for the apex. The change in filament length between its normal unperturbed state and the elongated state required to form the tent shape is used to evaluate the strain. The elongation is divided by the length of the filament from the impact position to the clamping point. Once the strain for each filament is determined, we can then use the stress-strain relationship from Sanborn [6] to calculate the total force experienced by the load cell. Published scanning electron

microscope data for Dyneema HB26 [10] was used to determine the size and distribution of the individual fibers within uniaxial layers. Figure 6 shows that over a length of 0.509 mm that there are four filament rows with an average filament diameter of 16.9 μm. Using the measured stress-strain value, at a strain rate of 1000 (1/s), we were able to develop a second-order polynomial relationship of the stress and strain experienced by each filament within this computational model. The complete LabVIEW program used for the simulation is available from the Physics Department Armor Systems Laboratory at NPS [2].

IV. DATA

The initial aim of the study was to build a data set of four samples with deflection and impact force measurements, one for each fabrication pressure (20.7 MPa, 13.8 MPa, 6.9 MPa and un-pressed). After completing the first seven trials, the set was complete and available for analysis. The first round of DIC failed to produce deflection measurements, the result of an inability of the software to correlating the speckle pattern between cameras of differing resolution and pixel size. Before it was understood that the issue was software based, a second set of trials was conducted using a less dense pattern and with matching camera resolution but not pixel size. In addition to the challenges in measuring deflection, it was also observed that the clamps were severing the fibers during impact loading. Samples used after Shot 7 were constructed using adhesive film and polyurea to protect the fibers. When the second data set also failed to produce deflection measurements with DIC, a final test shot was conducted using a mirror to collect the deflection measurement in the Z direction. Post-impact visual inspection identified Shot 5, 7, 8 and 11 as the only data sets with complete force and video recordings, as well as unbroken fibers at clamp locations. A complete record of all test shots, including the pre-fire conditions and record of observations made (force/video) can be found in Table 1.

Table 1. Record of Shots Fired

Shot #	Sample Pres (MPa)	Gun Pres (MPa)	Velocity (m/s)	Pre-Load X (N)	Pre-Load Y (N)	Mass (g)	Ref Distance (mm)	Force Data (Y/N)	Video (Y/N)
1	0	2.15	-	-	-	22.0	-	N	N
2	20.7	2.25	-	-	-	22.1	-	N	N
3	20.7	-	345	12	-1.5	21.9	75	Y	Y
4	13.8	2.15	285	13.5	-2	22.5	76	Y	N
5	6.9	2.25	305	8	1	22.3	75	Y	Y
6	0	2.25	315	13	-3	22.5	74	Y	Y
7	13.8	2.1	290	14	-5	22.4	74	Y	Y
8	20.7	2.1	-	6.5	0	21.8	105	Y	Y
9	13.8	2.15	-	12.5	1	22.4	74	Y	Y
10	6.9	2.15	-	13.5	3.5	22.4	73	N	Y
11	20.7	2.2	316	-	-	22.2	76	Y	Y

Data analysis required some additional measurements be taken for each test to identify the location of the point of impact. This included selection of a reference point to act as the origin for a coordinate system, and the location of the fabric clamps relative to the impact points to establish boundary conditions for wave propagation (Table 2). Table 3 contains the deflection measurements for the first eight video frames of Shot 11, at which point the front edge of the transverse wave broke the mirror used to view the impact.

Table 2. Impact Locations

Measurement	Distance to Impact Point (mm)			
	Shot 5	Shot 7	Shot 8	Shot 11
X Load Cell	134	134	135	134
X Clamp	150	148	146	147
Y Load Cell	144	145	148	145
Y Clamp	138	138	135	135
From Origin in X	30	30	32	29
From Origin in Y	40	40	42	41
Target Thickness	1.397	1.346	1.422	1.372

Table 3. Deflection Measurements Shot 11

Frame	Deflection (mm)
11-1	0.5
11-2	6.5
11-3	13
11-4	17.5
11-5	21
11-6	24.5
11-7	25.5
11-8	27.5

To determine the total strain in the fibers without DIC, the video of Shot 11 was used to measure the expansion of the transvers wave in each frame. By measuring the location of the vertices that form the deflection tent, a model could be built to estimate strain. Measurements were also taken for Shots 5, 7 and 8 to examine trends in wave propagation (Table 4).

Table 4. Transverse Wave Tent Propagation Measurements

Frame		Top (mm)		Bottom (mm)		Left (mm)		Right (mm)
5-1	X	31	X	31	X	13	X	49
	Y	56	Y	23	Y	40	Y	39
5-2	X	30	X	30	X	4	X	57
	Y	68	Y	15	Y	39	Y	40
5-3	X	29	X	30	X	-16	X	74
	Y	83	Y	-2	Y	39	Y	38
5-4	X	30	X	29	X	-27	X	83
	Y	95	Y	-9	Y	40	Y	39
7-1	X	30	X	30	X	12	X	49
	Y	55	Y	23	Y	39	Y	39
7-2	X	29	X	30	X	10	X	55
	Y	67	Y	17	Y	40	Y	40
7-3	X	29	X	30	X	-8	X	65
	Y	82	Y	5	Y	40	Y	40
7-4	X	29	X	29	X	-24	X	73
	Y	92	Y	-6	Y	40	Y	40
8-1	X	30	X	32	X	17	X	46
	Y	55	Y	27	Y	42	Y	42
8-2	X	29	X	32	X	6	X	57
	Y	67	Y	17	Y	42	Y	42
8-3	X	29	X	32	X	-3	X	65
	Y	82	Y	8	Y	41	Y	42
8-4	X	29	X	33	X	-11	X	78
	Y	92	Y	-3	Y	41	Y	42
11-1	X	29	X	29	X	15	X	44
	Y	54	Y	27	Y	41	Y	41
11-2	X	28	X	29	X	7	X	54
	Y	64	Y	16	Y	41	Y	41
11-3	X	30	X	28	X	-1	X	61
	Y	73	Y	8	Y	40	Y	42
11-4	X	27	X	29	X	-10	X	70
	Y	84	Y	-2	Y	40	Y	42

Load cell force data was recorded for eight of the eleven shots fired. Shot 3 was excluded because video showed the projectile missed the target area. Because the data included 500 samples for each shot, results are presented graphically for the first 150 time steps. Figure 14 contains graphs of the load cell data for Shot 4 – 9 and Figure 15 the results of Shot 11.

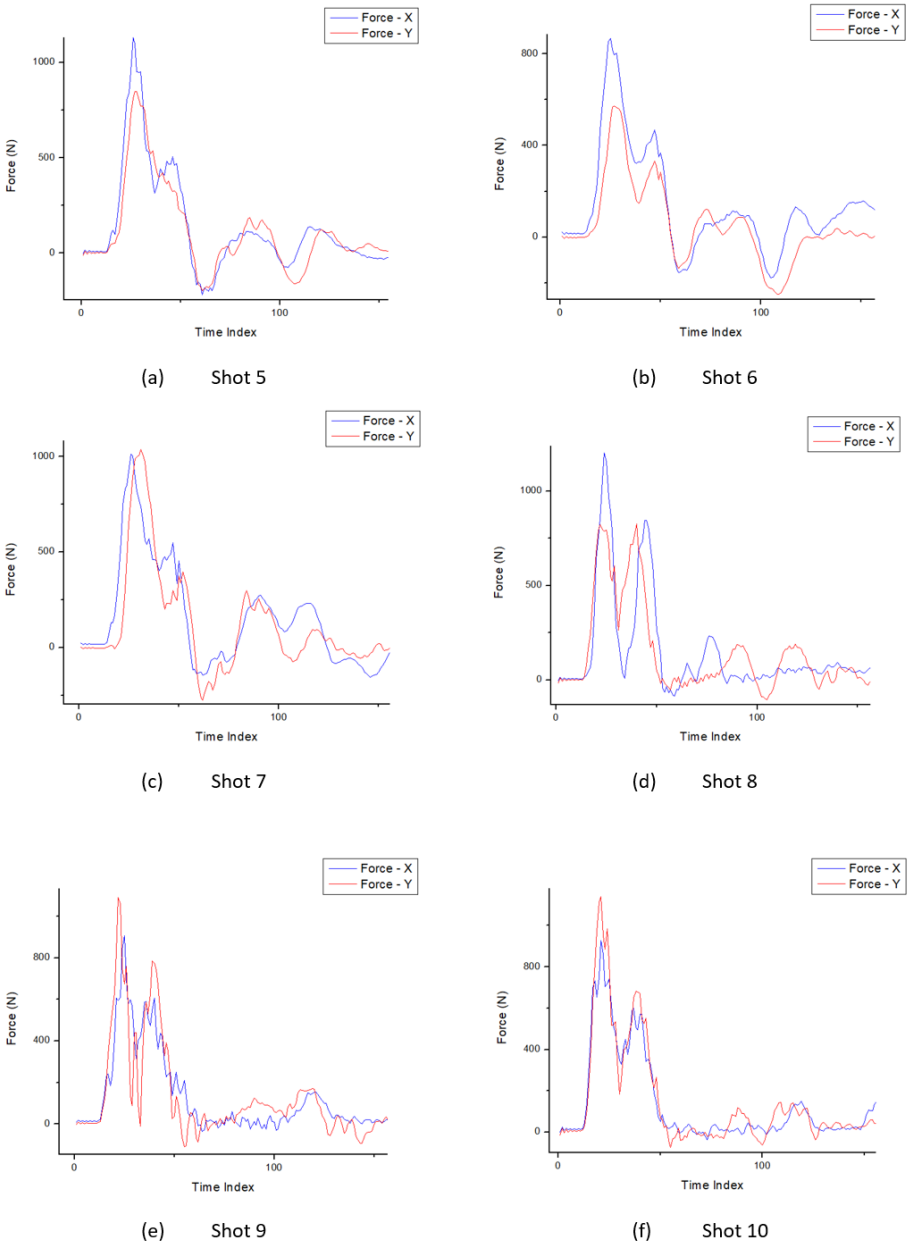

Figure 14. Load Cell Data

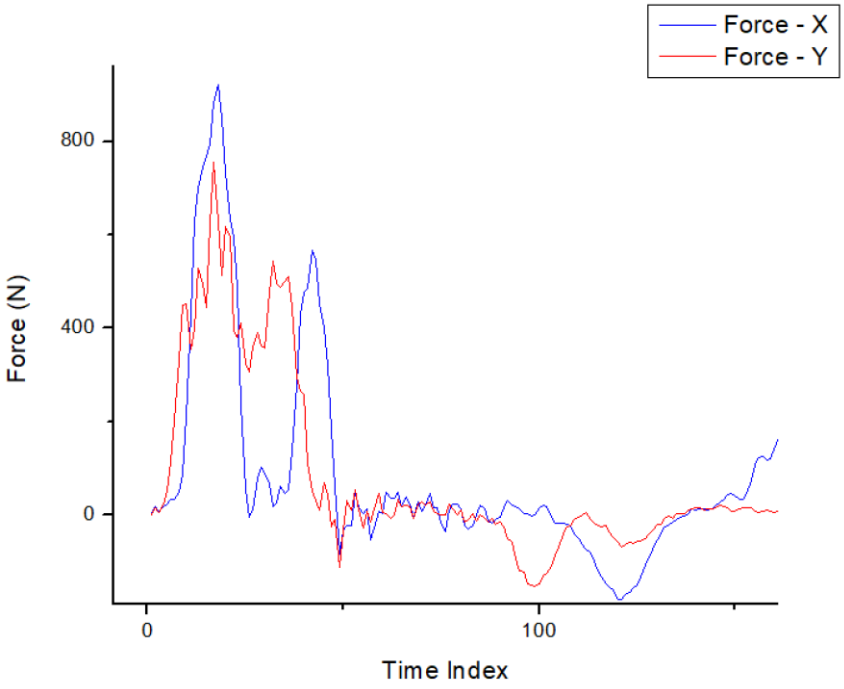

Figure 15. Load Cell Data—Shot 11

Target samples were collected after each impact and examined for signs of damage to the fibers at the impact site. Figure 16 shows the front and rear views of the samples for Shot 5, 7, 8 and 11. A forensic analysis was performed on each of the targets to determine how many layers were perforated. Starting from the impact face, layers were peeled back and examined and the number of broken or severed layers was recorded (Table 5). The results showed a slight correlation between pressure and damage, suggesting that increased processing pressures displayed reduced BFD but the projectile perforated deeper into the sample. This was difficult to confirm over the entire sample set due to the effect of the damage caused at the clamping site in the early tests.

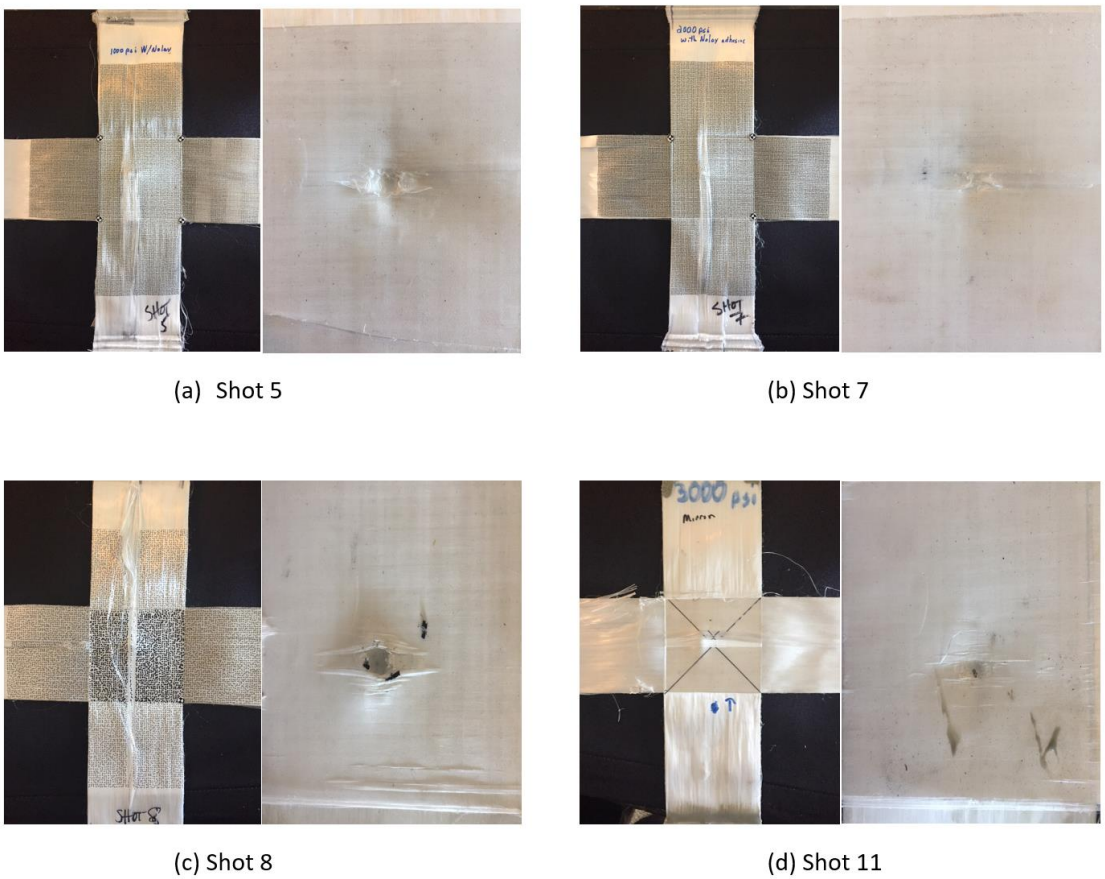

(a) Shot 5 (b) Shot 7

(c) Shot 8 (d) Shot 11

Figure 16. Target Sample Views—Post Impact

Table 5. Damage Results

Sample	# Damaged Layers
Shot 5 (6.9 MPa)	5
Shot 7 (13.8 MPa)	3
Shot 8 (20.7 MPa)	8
Shot 11 (20.7 MPa)	3

V. DATA ANALYSIS

The calculation of total strain experienced by an impacted target sample requires a mechanism for comparing the un-stretched and elongated lengths of each fiber in the sample. Unfortunately, DIC software was unsuccessful in providing the Z direction displacement data needed to provide a complete BFD profile for the test samples. Using the video of each impact, an approximation of the deformation tent geometry was constructed by tracking the vertices of the transverse wave as it propagated frame by frame. Progression of the tent expansion for Shot 5, 7, 8, and 11 can be seen in Figure 17. In the recorded video, two critical aspects of the analytical model proposed by Smith [3] can be verified: inward flow of the material towards the impact site in the X and Y direction, and transition of material flow from the axial direction of the fibers to the Z direction as the transverse wave passes. Measurement of the transverse wave velocity was possible by manually tracking the movement of the vertices from frame-to-frame (Table 6). The transverse velocity approximations have large statistical variance, primarily because the vertex locations were not obvious, and even slight deviations in position resulted in large variations of velocity. After four frames taken from the point of impact (less than 0.1 ms), the transverse wave had already passed out of the field of view. Overall, the data pointed to transverse wave velocities in the range of 500-650 m/s, but a higher frame rate would be required to refine the estimate. The data set shows an overall trend with a higher transverse wave velocity in the low-pressure samples, and decreased velocities as the processing pressure is increased.

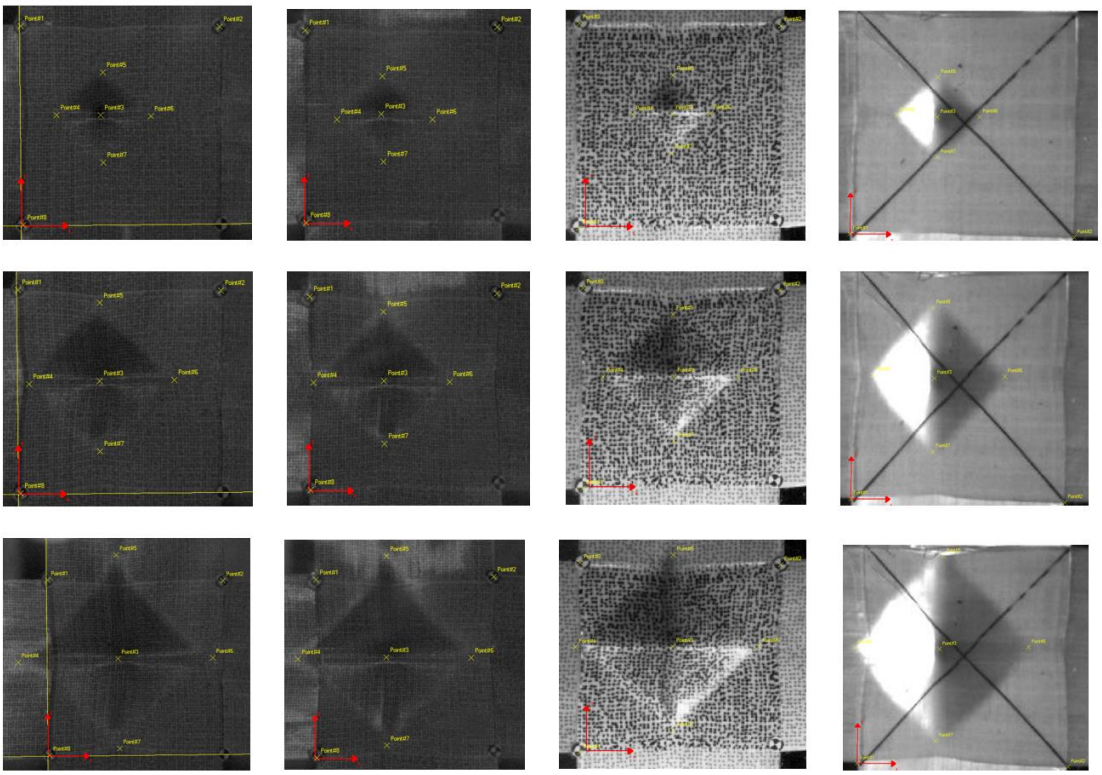

(a) Shot 5 (b) Shot 7 (c) Shot 8 (d) Shot 11

Figure 17. Transverse Wave Propagation

Table 6. Transverse Wave Velocities

Position	Frame	Transverse Wave Velocity (m/s)			
		Shot 5	Shot 7	Shot 8	Shot 11
Left	0-1	671	712	656	555
	1-2	735	500	471	421
	2-3	756	637	404	437
Top	0-1	582	662	585	583
	1-2	665	674	576	483
	2-3	741	627	731	495
Right	0-1	681	635	622	619
	1-2	642	391	475	447
	2-3	632	439	520	410
Bottom	0-1	628	574	616	611
	1-2	608	449	481	462
	2-3	608	579	520	464
Left	Avg	721	616	510	471
Top	Avg	663	654	631	520
Right	Avg	652	488	539	492
Bottom	Avg	615	534	539	512
Total	**Avg**	**662**	**573**	**555**	**499**
Variance	Above	94	139	176	120
	Below	-80	-182	-151	-89

The BFD profile of each sample was extrapolated from the deflection data recorded in Table 3, which tracked the apex of the deformation tent. The progression of the apex in the Z direction for Shot 11 can be seen in Figure 18. Using the LabVIEW numerical simulation for the tent geometry discussed in Chapter 3, a summation of the total strain in the target sample was made for each image frame. The strain, representing the change in fiber length divided by the original fiber length, was correlated with the stress-strain curves in Figure 2 using a polynomial relationship.[3] Once a stress value (Pa) for a differential element of the tent width is obtained for the surface layer, it is multiplied by the number of fibers in the thickness of the layer, then summed across the tent width and applied to all layers. The process is repeated for the X and Y directions. The stress is multiplied by the

[3] Curves were fitted to the polynomial $Y = A + Bx + Cx^2$ with the following coefficients: A = 1.2372x107, B = 1.39745x1010, and C = -8.45477x1010. Y is calculated in units of Pa and x represents the strain measurement for each differential width in the tent cross-section.

cross-sectional area of an individual fiber to convert into a force (N) measurement. The summation of forces in each direction was then compared to the force measurements obtained from the load cell to validate the stress-strain relationship model against the experimental data (Table 7). Although the variance in the first two frames is high, the progression of the force over time shows a strong correlation with the experimentally measured data. Without deflection measurements for any additional samples, the accuracy of the predictive model will require further testing to verify.

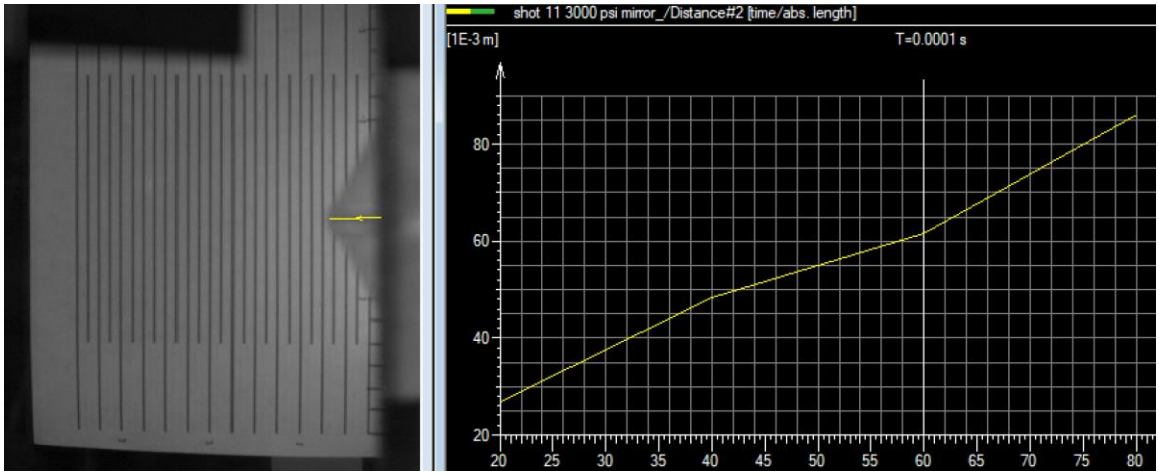

Figure 18. Deflection Apex Progression

Table 7. Force Comparison

Frame	Calculation N		Measurement N		Variance |N|	Variance %
11-1	X	16.55	X	33.36	16.81	101.6
	Y	14.01	Y	5.43	8.58	61.2
11-2	X	17.61	X	33.36	15.75	89.4
	Y	19.57	Y	23.98	4.41	22.5
11-3	X	47.77	X	49.38	1.61	3.4
	Y	54.54	Y	52.71	1.83	3.4
11-4	X	81.71	X	87.45	5.74	7.0
	Y	94.35	Y	114.19	19.84	21.0

Analysis of the load cell force data in Figures 14 and 15 provided further insight into the behavior of the samples post-impact. After accounting for the offset in the X and Y curves related to the off-center impact, the non-symmetrical boundary conditions, and the breakage of fibers at the clamping sites, a generalized pattern of behavior was visible in all curves. A generic representation of the impact force over time is shown in Figure 19. There are several key points of interest consistent to all graphs presented in the research. First is the initial impact point. The wave speed of the elastic wave far exceeds the transverse wave propagation, and was confirmed visually by the movement of the fibers inward toward the impact site ahead of the deformation tent. As a result, the force measurements increase dramatically at the start of the material deformation. The second critical point is the max force experienced at the load cell. When compared with the video, this appears to coincide with the time when the transverse wave makes contact with the clamping site boundary. At this point a transverse refraction wave is visible returning toward the impact site. There are two possible explanations for the max force value: the reflection wave creates a relief of tension at the clamping site, or the projectile has completely decelerated. Without deflection data that would indicate the residual velocity of the projectile, it cannot be determined which mechanism is causal. As the force reduces, two additional inflection points occur that result in a local min and max on the data curve. When compared with the video, this appears to coincide with the transverse wave fronts crossing on the target sample. This would result in constructive and destructive interference that would affect tension in the fibers. The final region of interest is the oscillation of the force value above and below zero, characterized in the video by the displacement of the target in the positive and negative Z direction until equilibrium is restored. The consistency in the force data, coupled with the correlation with the predicted force results, suggests that future testing to capture the BFD profile will provide an accurate model of the propagation of forces by the fibers.

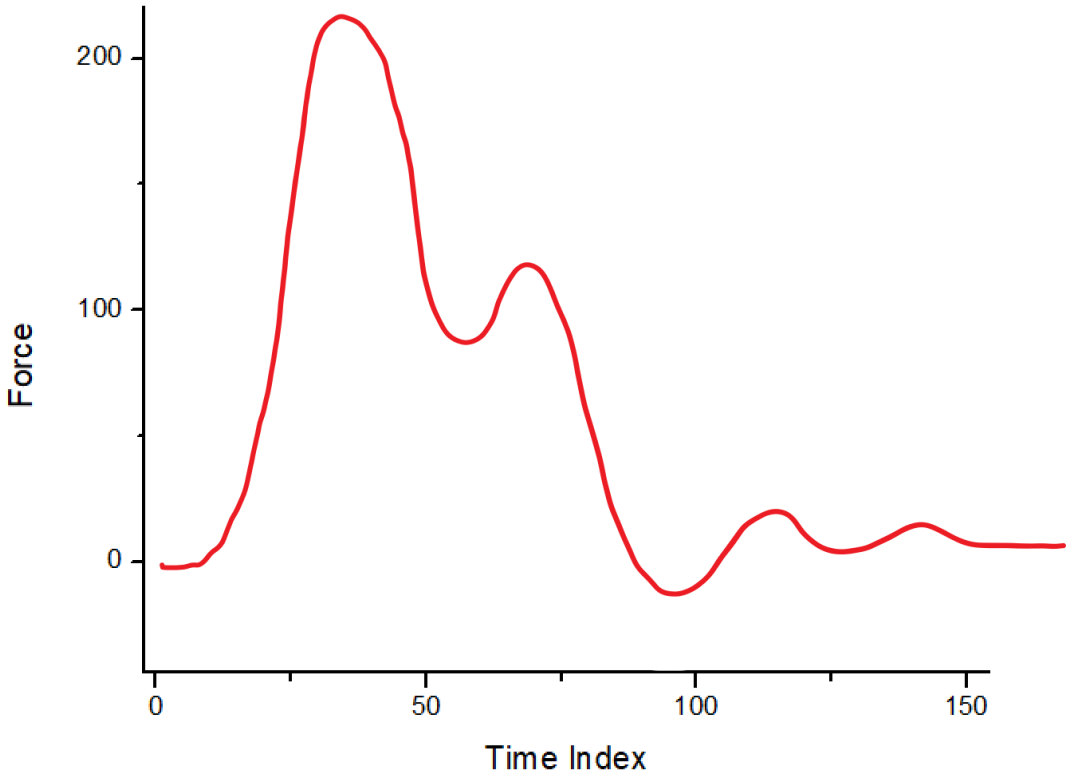

Figure 19. Generic Uniaxial Force Curve

VI. CONCLUSION

The goal of this research was to develop an experimental tool to evaluate the stress-strain behavior of textile armor systems under ballistic loading When the study was completed, the correlation between the predicted force values of the model and the experimental measurements were sufficiently close to validate the experimental design. In the process, many of the technical challenges encountered were overcome and will enable future research to complete a full set of measurements at each sample pressure. A key discovery was the ability to construct a multi-layered textile target with no inter-layer fabric slippage and no shearing of the fibers at the clamping sites.

In this research, four samples met the criteria of zero visible shearing at the clamping sites. Those samples were analyzed for impact damage and determination of transverse wave velocities. Results showed between 3 – 8 layers of perforation damage at the site of the projectile. Correlation between processing pressure of the samples and fiber damage was inconclusive. Transverse wave velocities ranged between 500-650 m/s, and were observed to be inversely proportional to the fabrication pressure. Deflection data was limited to a single impact test, and could be matched with the transverse wave data for only four image frames. The resulting force comparison between the predictive model and the experimental measurement showed a strong correlation despite the limited data set. Of the eight values predicted by the numerical simulation, experimental measurements were within 7% of the expected value on three occasions. Additional testing is required to demonstrate the accuracy and repeatability of the model.

Several modifications to the experimental setup are recommended to create a more accurate BFD profile and total strain measurement. Issues with the DIC software, specifically its failure to track unique patterns in cameras of differing resolution and pixel size, limited the ability to obtain deflection data in the Z direction. The software provider is currently resolving the problem and future trials using DIC will provide a more accurate and detailed representation of the actual BFD. Additionally, it is recommended that a higher frame rate be used to record the event. This will reduce the error in the calculation of the transverse wave velocity, and assist with the tracking of points between frames.

Target mounting would be improved with a mechanism to align the center of the sample with the gas gun bore to create a more consistent distance between the four clamping sites.

The consistency in the load cell force data curves, coupled with the close correlation between the predicted and observed results suggests that the model will produce accurate results in forthcoming tests. Future research should focus on reducing the variance in measured data, and generation of a complete data set for the BFD profile that can be used to calculate total strain over a longer period post-impact. Once all of the identified issues with the current system have been addressed, this application can be applied to various front-face armor materials positioned in front of the fabric target for a complete system level performance assessment of composite combinations. Ideally, this system will be used to identify the performance of front-face armor systems against specific projectiles, with a view to reduce the overall load experienced by the textile armor backing.

LIST OF REFERENCES

[1] B. Scott, Fiber-based materials in body armor," in *Army Research Labs Presentation*, Monterey, March 10, 2017.

[2] R. Gamache, *(unpublished)* Naval Postgraduate School Research, 2017.

[3] J. C. Smith, F. L. McCrackin and H. F. Schiefer, "Stress-Strain Relationships in yarns subjected to rapid impact loading," *Textile Research Journal*, no. April, pp. 288–302, 1958.

[4] T. von Karman and P. Duwez, "The propagation of plastic deformation in solids," *Journal of Applied Physics*, vol. 21, no. 10, pp. 987–994, 1950.

[5] B. Cheesman and T. Bogetti, "Ballistic impact into fabric and compliant composite laminates," *Composite Structures,* vol. 61, pp. 161–73, 2003.

[6] B. Sanborn, A. DiLeonardi and T. Weerasooriya, "Tensile properties of Dyneema SK76 single fibers at multiple loading rates using a direct gripping method," Army Research Labs, 2014.

[7] I. S. Chocron-Benloulo, J. Rodriguez and V. Sanchez-Galvez, "A simple analytical model to simulate textile fabric ballistic impact behavior," *Textile Research Journal,* vol. 67, no. 7, pp. 520–528, 1997.

[8] V. B. C. Tan, C. T. Lim and C. H. CHeong, "Perforation of high-strength fabric by projectiles of different geometry," *International Journal of Impact Engineering,* vol. 28, pp. 207–222, 2003.

[9] L. Vargas-Gonzales, "Ballistic modification of ultra-high molecular weight polyethylene composites through processing," U.S. Army Research Laboratory, Aberdeen.

[10] DSM, "Dyneema HB26 specification sheet." [Online]. Available: https://www.dsm.com/

[11] OMEGA, "LCHD Load Cell Specification Sheet." [Online]. Available: https:// www.omega.com/pressure/pdf/LCHD.pdf

[12] Whithner, “Triggerbox 1000 specification sheet.” [Online]. Available: www.whithner.com/images/TRIGGER-SCREEN-BROCHURE.pdf.

[13] BNC, “577 Pulse Generator specification sheet.” [Online]. Available: https://www.berkeleynucleonics.com/sites/default/files/products/datasheets/577-ds-5-2-18.pdf

[14] NI, “9237 Signal Conditioner specification sheet.” [Online]. Available: http://www.ni.com/pdf/manuals/374186a_02.pdf

[15] Phantom, “V2512 specification sheet.” [Online]. Available: https://www.phantomhighspeed.com/Portals/0/Docs/DS/DS_WEB-UHS-vXX12-Family.pdf?ver=2017-07-11-085549-743

[16] Shimadzu, “HPV-X2 specification sheet.” [Online]. Available: https://www.ssi.shimadzu.com/sites/ssi.shimadzu.com/files/Products/literature/testing/C220-E015C.pdf

[17] Phantom, “V711 specification sheet.” [Online]. Available: https://www.phantomhighspeed.com/Portals/0/Docs/Products/DS_WEB-1Mpx%20v-Series.pdf?ver=2016-02-01-084321-463

INITIAL DISTRIBUTION LIST

1. Defense Technical Information Center
   Ft. Belvoir, Virginia

2. Dudley Knox Library
   Naval Postgraduate School
   Monterey, California